Journal of King Saud University - Science 36 (2024) 103015

HOSTED BY

ELSEVIER

Contents lists available at ScienceDirect

Journal of King Saud University - Science

journal homepage: www.sciencedirect.com

Original article

Zn-modified In_2O_3 nanoparticles: Facile synthesis, characterization, and selective cytotoxicity against human cancer cells

ZabnAllah M. Alaizeri *, Hisham A. Alhadlaq, Mohd Javed Akhtar, Saad Aldawood

Department of Physics and Astronomy, College of Science, King Saud University, Riyadh 11451, Saudi Arabia

ARTICLE INFO

Keywords:
Precipitation process
Zn doping
Anticancer activity
Physicochemical properties
Selective cytotoxicity

ABSTRACT

Oxide nanoparticles (NPs) have attracted considerable interest owing to their unique characteristics and possible applications, including gas detection, bioanalytical sensing, catalytic, and biomedical. The present work was designed to explore the effect of varying amounts (2.5 %, 5 %, and 7.5 mol%) of Zn-doping on the properties and selective anticancer efficacy of In_2O_3 NPs. The precipitation process was applied to prepare pure In_2O_3 NPs and Zn-doped In_2O_3 NPs. XRD, TEM, SEM, EDX, XPS, UV–Vis, and PL techniques have been employed to investigate the physicochemical properties of NPs. The XRD analysis revealed that the crystallite of the In_2O_3 lattice was slightly changed with the addition of Zn ions. TEM and SEM images displayed that the reduction of size of In_2O_3 NPs was increased with increasing Zn concentrations. The composition elements and distribution of Zn dopants within In_2O_3 NPs were further confirmed by EDX and XPS techniques. Based on the UV–Vis study, increasing the Zn amount improved the gap energy of In_2O_3 NPs by shifting edge absorption peaks to lower wavelengths. Moreover, PL spectra show that the intensity of In_2O_3 NPs decreased with increasing the Zn amount. The biological results indicate that the Zn-doped In_2O_3 NPs exhibited a significant increase in cytotoxicity with Zn doping increased against MCF-7 and HCT116cells while they have excellent biocompatibility with normal human cells (HUVECs). These results suggest that these NPs hold promise as a novel therapeutic approach in cancer treatment. This study requires more research into the biological applications of Zn-doped In_2O_3 NPs.

1. Introduction

Nanotechnology has attracted interest in the biomedical field as a novel approach for addressing some challenges in healthcare problems, such as drug delivery and cancer therapy (Jahan, 2022; Patel and Nanda, 2015; Sun et al., 2014;). Currently, enhanced nanomaterials provide tailored cancer therapies that maximize therapeutic efficiency owing to their superior properties (Gao et al., 2019; Navya et al., 2019). Oxide nanoparticles (NPs) are now being studied of significant interest within nanomaterials due to their exceptional mechanical, electronic, and catalytic characteristics. These properties make them very promising in potential applications such as sensing, electronics, and biomedicine (Malini et al., 2022; Mishra et al., 2017; Sheena et al., 2019). For example, Indium oxide (In_2O_3) is a crucial n-type semiconductor with a band gap ranging from 3 to 3.75 eV (Bierwagen, 2015). Owing to its biocompatibility, low toxicity, and tunable bandgap, it has emerged as an attractive candidate in potential applications, including industrial, catalytic, electronics, and biomedical applications (Alaizeri et al., 2022a; Li et al., 2020; Yang et al., 2022).

The doping of oxide NPs has opened new research paths in numerous fields. For example, doping oxide NPs with transition metal ions can significantly affect their physicochemical properties and performance (Ahamed et al., 2016). For instance, In_2O_3 NPs NPs have been doped with metal ions (e.g., Zn, Co, and Ag) to improve their properties ("Ac ce d M us," 2019; Sun et al., 2016; Yan et al., 2018). Different physical, chemical, and biological approaches were successfully applied to achieve doping In_2O_3NPs with transition metal ions (Kulkarni and Patil, 2016; Naik and Salker, 2017). Shanmuganathan et al. (Shanmuganathan et al., 2021) reported that a 1 wt% of Mn, Fe, Co, Ni, and Cu were doped to In_2O_3 nanostructures using a hydrothermal process to enhance photocatalytic activity. In another study, Sn-doped In_2O_3 NPs synthesized using a sol–gel combustion method (Ayeshamariam et al., 2014).

Several studies are attracting attention in using metal-doped oxide NPs in biomedicine applications because to their superior properties. However, modifying these NPs with zinc (Zn) can enhance their properties, potentially improving their efficacy in cancer therapy. Sharma et al. (Sharma et al., 2022) investigated that Zn doping improves the physicochemical characteristics of WO_3 NPs for biosensing, imaging,

* Corresponding author.
E-mail address: zalaizeri@ksu.edu.sa (Z.M. Alaizeri).

https://doi.org/10.1016/j.jksus.2023.103015
Received 15 August 2023; Received in revised form 12 November 2023; Accepted 16 November 2023
Available online 18 November 2023

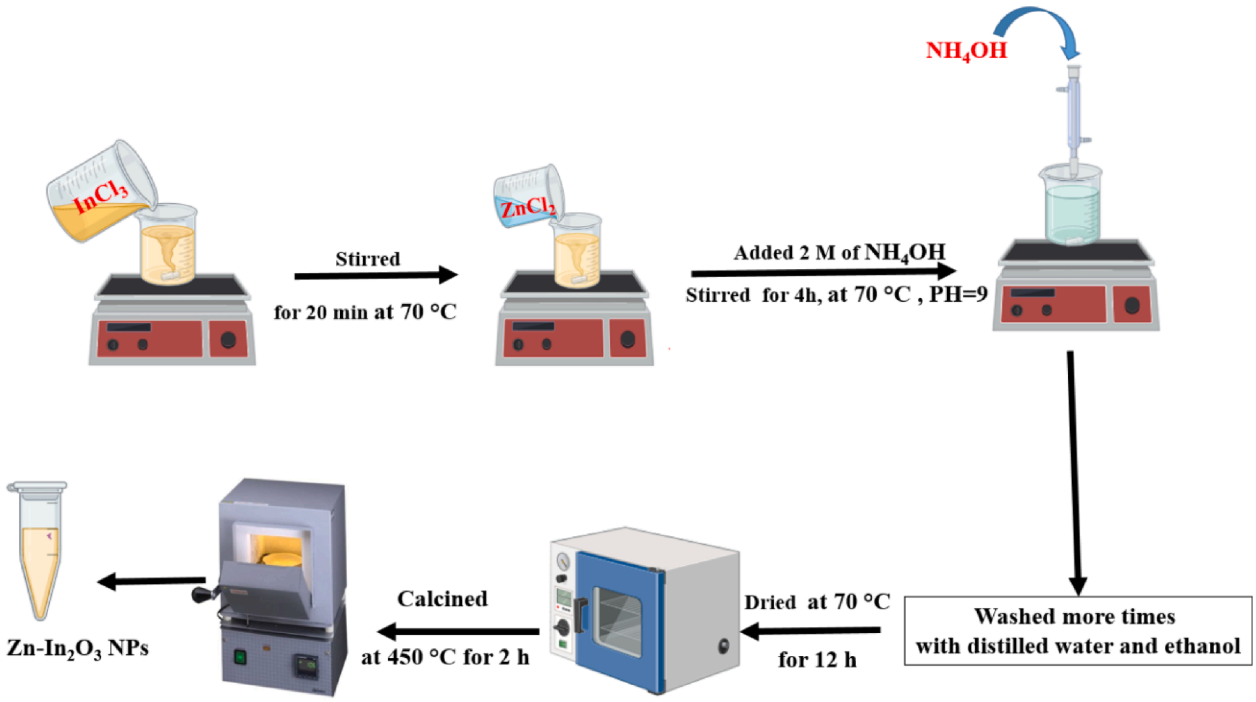

Scheme 1. The procedure of synthesis of Zn-doped In_2O_3 NPs.

antibacterial, and anticancer medicine. Darvish et al. (Darvish et al., 2022) observed that human lung (A549) cancer cells responded better to doping Zn on $CuFe_2O_4$ NPs than to $CuFe_2O_4$ NPs. The improved therapeutic efficacy and reduced systemic toxicity by using Fe-doped ZnO NPs in a murine tumor model demonstrated by Zhao et al. (Zhao et al., 2018). Our previous work (Alaizeri et al., 2022a) investigated that the Ag adding has a role in the improved photocatalytic and anticancer performance of In_2O_3 NPs. Additionally, Karmaoui et al. (Karmaoui et al., 2016)found that Pt-decorated In_2O_3 NPs display high sensitivity in detecting acetone and a biomarker for diabetes. Vázquez-Olmos et al. (Vázquez-Olmos et al., 2014)synthesized Mn-doped In_2O_3 NPs and found evidence of paramagnetic centers, suggesting potential applications in diluted magnetic semiconductor.

The goal of the present work was to evaluate the influence of Zn doping on the physicochemical and anticancer properties of In_2O_3 NPs. Pure In_2O_3 NPs and Zn-doped In_2O_3 NPs were prepared through chemical precipitation. The physicochemical properties of the prepared NPs were investigated through XRD, TEM, SEM, EDS, XPS, UV–vis, and PL Spectrometer. Anticancer activity of synthesized NPs was evaluated using different types of human cancer cells (MCF-7 and HCT116). Furthermore, the biocompatibility of the prepared nanoparticles was assessed by the normal HUVE the cells. In vitro study results showed that In vitro study showed that Zn doping increases selective anticancer efficacy of In_2O_3 NPs against human normal (HUVEs) and different types of cancer cells(MCF-7 and HCT116).

2. Experimental details

2.1. Chemicals, reagents, and cells

Indium chloride ($InCl_3$) (purity of 98 %), zinc chloride ($ZnCl_2$) (minimum purity of 98 %, and ammonium hydroxide (NH_4OH) (a concentration of 28.0–30.0 % NH_3 basis) were supplied from Sigma Aldrich (Millipore-Sigma, St. Louis, MO, USA). MTT (6-[4,5-dimethylthiazol-2-yl]-2,5-diphenyl-tetrazolium bromide), and foetal bovine serum (FBS) were provided from Sigma Aldrich (Millipore-Sigma, St. Louis, MO, USA). The human breast (MCF-7) and colorectal (HCT116) cancer cells were acquired from the American (ATCC, Manassas, West Virginia, USA). The normal human umbilical vein endothelial cells (HUVECs) were received from the microbiology Lab at King Saud University (KSU).

2.2. Synthesis of Zn-doped In_2O_3 NPs

Zn-doped In_2O_3 NPs were successfully synthesized using a chemical precipitation process as in an earlier study (Zheng et al., 2021). The 3.6 mmol of indium chloride ($InCl_3$) was prepared in 20 ml of ethanol and 10 ml of distilled water under stirring for 20 min at 70 °C on a hot plate. Next, different amount (2.5 %, 5 %, and 7.5 mol%) zinc chloride ($ZnCl_2$) was dropwise added to the solution with stirring. After that, a 2 M solution of ammonium hydroxide (NH_4OH) was also gradually added to reach a pH of around 9 under continuous stirring for 4 h to get precipitate. Subsequently, The precipitate was rinsed repeatedly with distilled water and ethanol and centrifuged at 7000 rpm for 5 min to separate it from the solution. The rinsed precipitate was then dried at 70 °C for 12 h and annealed at 450 °C for 2 h. At a similar protocol, pure In_2O_3 NPs were successfully synthesized. The above procedure of synthesis of Zn-doped In_2O_3 NPs was illustrated in Scheme 1.

2.3. Characterization

X-ray diffraction (XRD) patterns (PanAnalytic X'Pert Pro from Malvern, UK, with Cu-Kα radiation (wavelength = 0.15405 nm) at 45 kV and 40 mA) were used to examine phases and crystal structure of prepared NPs. Moreover, field emission transmission electron microscopy (FE-TEM) (JEM-2100F, JEOL, Inc., Tokyo, Japan) was used to determine particle size of NPs. Moreover, field emission scanning electron microscopy (FE-SEM) (JSM-7600F, JEOL,93Inc) was applied to investigate shape and surface morphology of these NPs. We used EDX and XPS (PHI-5300 ESCA PerkinElmer, Boston, MA) to confirm elemental amnalysis and chemical states of samples. UV–Visible spectrometer (Hitachi U-2600) and PL spectrometer (Hitachi F-4600) were employed to measure optical characteristics.

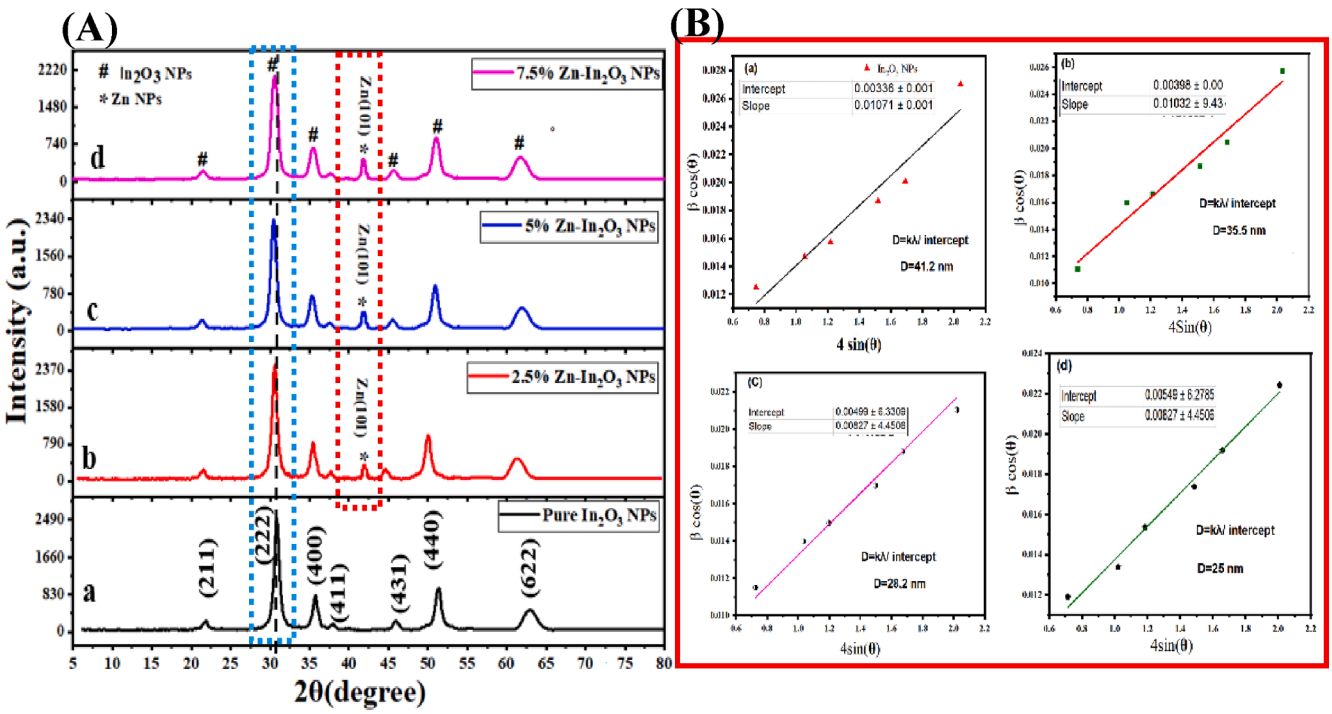

Fig. 1. XRD spectra (A): undoped In_2O_3 NPs (A), Zn (2.5 %)-In_2O_3 NPs (b), Zn (5 %)-In_2O_3 NPs (c), Zn(7.5 %)-In_2O_3 NPs (d), and Williamson-Hall (W-H) plot (B): undoped In_2O_3 NPs (a)and Zn (2.5 %)-In_2O_3 NPs (b), Zn (5 %)-In_2O_3 NPs (c), and Zn(7.5 %)-In_2O_3 NPs (d).

2.4. Cells culture

MCF-7 and HCT116 cancer cells were cultured in Dulbecco Modified Broker Eagle Medium (DMEM) with 10 % fetal bovine serum (FBS) and antibiotics (100 µg/mL streptomycin and 100 U/mL penicillin). Cells were maintained in anincubator at 37 °C with 5 % CO_2. Similarly, the normal human umbilical vein endothelial cells (HUVECs) were also cultured at same conditions.

2.5. Exposure of cells to NPs and MTT bioassay

A stock solution of obtained NPs at 1 mg/mL was prepared using a culture medium (DMEM) as a solvent. In each sample, the stock solution was diluted to varying concentrations (1.5, 5, 10, 25, 50, 100, 200, and 300 µg/m). The suspension solutions were sonicated at 40 kHZ for 30 min to avoid NPs aggregation. A 96-well plate with 1×10^5 cells/mL was incubated at 37 °C with 5 % CO_2 for 24 h. Then, the cells were treated to varying concentrations (1.5–300 µg/mL) at 37 °C with 5 % CO_2. Then, a 10 µL of MTT solution was added into each well and placed to incubate for 3 h. At last, a volume of 100 µL of Dimethyl sulfoxide (DMSO) was utilized to solubilize the live cell formazan crystals present in each well. The cytotoxicity of NPs was determined by formazan solution absorbance at 570 nm.

2.6. Statistical analysis

ANOVA-way was successfully used in statistical analysis to establish the significance of the observed differences. P-value ($P < 0.05$) indicates statistical significance.

3. Results and discussion

3.1. Crystallographic structure

Fig. 1A(a-d) demonstrates the XRD spectra of undoped In_2O_3 NPs and Zn (2.5 %, 5 %, 7.5 %)-doped In_2O_3 NPs. In undoped In_2O_3 NPs, XRD peaks at 2θ values were located at 21.7°, 30.8°, 35.7°, 37.9°, 45.6°, 51.3°, and 62.8°, corresponding to the cubic bixbyite structure of (211), (222), (400), (411), (431), (440) and (622) planes. Furthermore, It can be seen in (Fig. 1b), the new peak (101) plane at 42° is related to Zn metal. The shift of peaks to lower angles (2θ) compared to the undoped In_2O_3 NPs indicates the incorporation of Zn into the In_2O_3 lattice as agreed with earlier studies (Huang and Lin, 2012; Samerjai et al., 2016). This shifted could be attributed to Zn ionic radii (0.074 nm) smaller than In ionic radii (0.122 nm)(Ahmed et al., 2021; Alahsab et al., 2023). Similarly, the XRD spectra of Zn (5 % and 7.5 %)-doped In_2O_3 NPs (Fig. 1A(c and d)) displayed changes in peak positions and intensities that increased with increasing concertation of Zn doping. These variations were associated with the changes in the crystallographic arrangement outstanding to the existence of Zn in the In_2O_3 lattice (Li et al., 2014; Martha et al., 2014). Furthermore, the In_2O_3 NPs XRD pattern has been matched to the cubic crystal structure (JCPDS card on 01-089-4595)(Koo et al., 2014; Zhang and Zhang, 2012). Using the XRD parameters, the average crystal sizes of the NPs were further estimated by the Scherrer equation. It can be shown in Table 1 that the average crystallite sizes of undoped In_2O_3 NPs and Zn (2.5 %, 5 %, and 7.5 %)-doped In_2O_3 NPs were decreased from 37.2 nm to 18.3 nm with increasing Zn amount as reported with the previous study (Shanmuga Priya et al., 2017). In comparison (Table 1), the average crystallite sizes of undoped In_2O_3 NPs and Zn (2.5 %, 5 %, 7.5 %)-doped In_2O_3 NPs using W-H method were found to be 42.1 nm, 35.5 nm, 28.2 nm, and 25 nm, respectively as displayed in Fig. 1B(a-d). XRD results suggested that the

Table 1
The structural properties of undoped In_2O_3 NPs, Zn (2.5 %)-In_2O_3 NPs, Zn (5 %)-In_2O_3 NPs, Zn(7.5 %)-In_2O_3 NPs.

Sample	Scherrer Method (nm)	W-H(nm) Method	TEM (nm)
In_2O_3 NPs	37.2	41.2	29
Zn (2.5 %)-In_2O_3 NPs	30.1	35.5	20.2
Zn (5 %)-In_2O_3 NPs	25.4	28.2	18.3
Zn(7.5 %)-In_2O_3 NPs	18.3	25	17.4

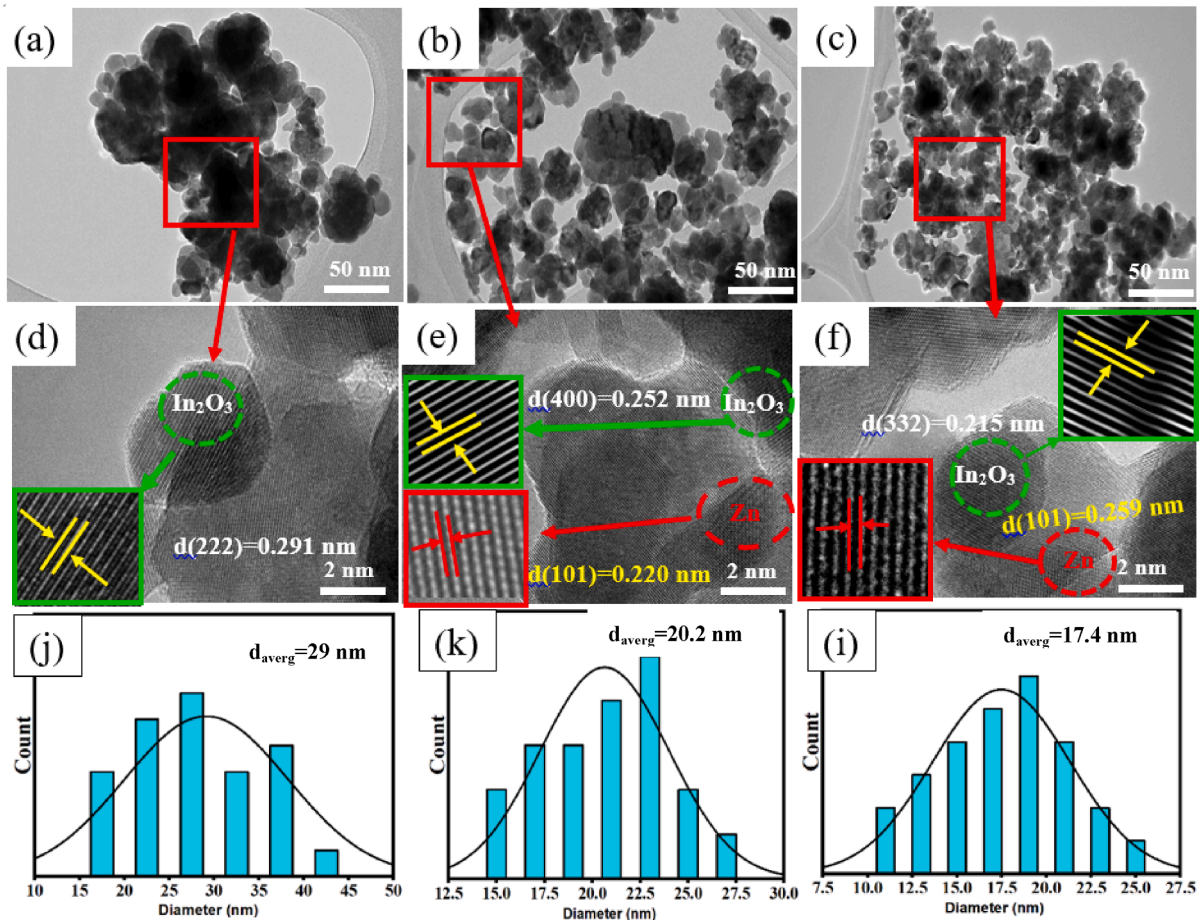

Fig. 2. TEM images of undoped In_2O_3 NPs and Zn(2.5 and 7.5 %)- In_2O_3 NPs (a-c), HR-TEM images of undoped and Zn(2.5 and 7.5 %)- In_2O_3 NPs (d-f), and the particle size distribution of undoped and Zn(2.5 and 7.5 %)- In_2O_3 NPs.

Zn doping plays a role in changes in peak positions, intensities, and widths in the In_2O_3 lattice, which influences the crystal structure.

3.2. TEM analysis

The growth behavior and morphologies of synthesized samples were further examined using the FETEM technique. As shown in Fig. 2(a-c), the particles of undoped and Zn (2.5 and 7.5 %)-doped In_2O_3 NPs were spherical shape and have less agglomeration and uniform distribution compared to as reported by many investigators (Shokohmanesh and Jamali-Sheini, 2017a). Moreover, HR-TEM images of prepared undoped In_2O_3 NPs and 2.5 % and 7.5 % Zn-doped In_2O_3 NPs are presented in Fig. 2 (d-f), respectively. We observed that d-spacing between adjacent lattice in undoped In_2O_3 NPs and Zn (2.5 and 7.5 %)-doped In_2O_3 NPs was 0.291 nm, 0.252 nm, and 0.215 nm, matching to the (222), (400), and (332) plane of In_2O_3, respectively. Additionally, the d-spacing values of the lattice in Zn metal were 0.220 nm and 0.259 nm, corresponding to the (101) planes (Ahamed et al., 2016). These results were in agreement with XRD data (Fig. 1A) and our previous study (Alaizeri et al., 2022b). Fig. 2(j-i) depicts in the histogram of particles the size distribution of In_2O_3 NPs and 2.5 % and 7.5 % Zn-doped In_2O_3 NPs. Table 1 showed that the average particle sizes of synthesized samples decreased (from 29 nm to 17.44 nm) with increasing Zn concentrations, as agreed with this study (Shanmuga Priya et al., 2017).

3.3. SEM with EDX analysis

The SEM images and EDX spectra of undoped In_2O_3 NPs and Zn(2.5 % and 7.5 %)-doped NPs were presented in Fig. 3(a-d). These images provide insights into the shape and morphology of the undoped In_2O_3 NPs and Zn-doped In_2O_3 NPs. Fig. 3(a-c) demonstrated that the particles of undoped In_2O_3 NPs were spherical in shape and had high aggregation homogenously compared to 2.5 % and 7.5 % Zn doped. This suggests that Zn doping at higher concentrations influences the growth and aggregation behavior of undoped In_2O_3 NPs. EDX spectra (Fig. 3 d) revealed oxygen (O), zinc (Zn), and indium (In) in Zn(7.5 %)-doped In_2O_3 NPs. Besides, the obtained percentages (Fig. 3 d) of the elements were good compatibility with the precursor used in the synthesis of 7.5 % Zn-doped In_2O_3 NPs. These values agree with XRD spectra (Fig. 1A). SEM elemental mapping (O, Zn, and In) in Zn (7.5 %)-doped In_2O_3 NPs is shown in Fig. 4(a-d). However, elemental mapping (Fig. 4b) confirmed the distribution of oxygen(O), Zinc(Zn), and indium (In) atoms within Zn (7.5 %)-doped In_2O_3 NPs. These results indicated that Zn doping in undoped In_2O_3 NPs was successfully prepared. SEM results agreed with XPS results (Fig. 5a) and agreed with many studies (Bouhdjer et al., 2016; Inyawilert et al., 2016; Zhu et al., 2020).

3.4. XPS analysis

Fig. 5a shows the full scan of XPS spectra that revealed distinct peaks corresponding to In, Zn, and O elements. Furthermore, this spectrum confirmed the successful incorporation of Zn dopants into the In_2O_3 NPs. Fig. 5(b-d) showed that the high-resolution spectra were performed to determine the binding energies (B.E) and chemical states of In 3d, Zn 2p, and O 1s elements. As displayed in Fig. 5b, the In3d spectra showed typical doublets for $In3d_{5/2}$ and $In3d_{3/2}$ at 444.20 and 451.72 eV, respectively, which provided with prior investigations (Khan et al., 2020; Zhang et al., 2016). The primary peaks found at 1022.25 eV and

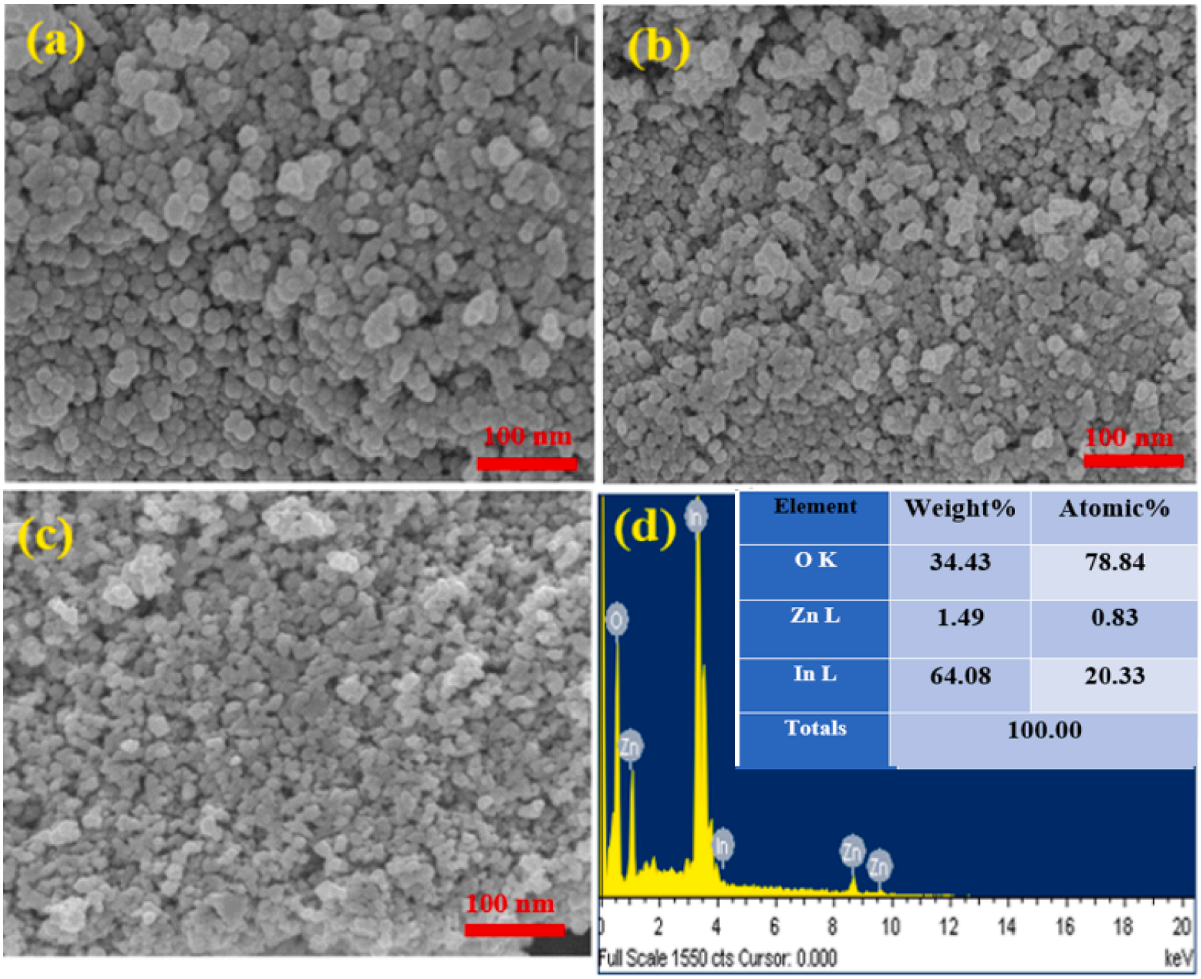

Fig. 3. SEM images of undoped In_2O_3 NPs(a), Zn (2.5 %)-doped In_2O_3 NPs (b), Zn (7.5 %)-doped In_2O_3 NPs(c), EDX spectra of Zn (7.5 mol%)-doped In_2O_3 NPs (d).

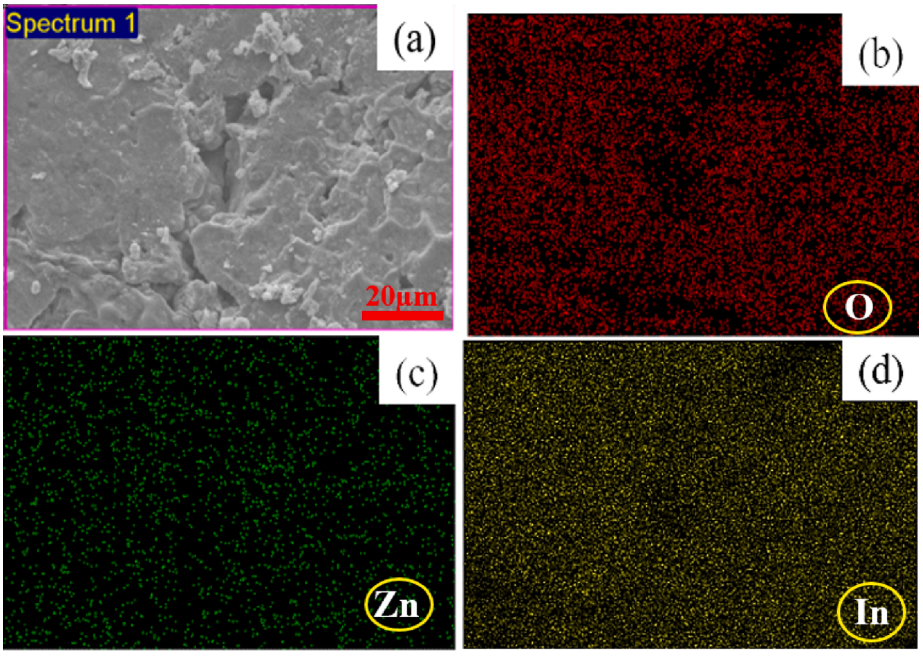

Fig. 4. SEM elemental mapping of Zn(7.5 %)- In_2O_3 NPs: Electron image(a), Oxygen(O) (b), Zinc (Zn) (c), Indium (In) (d).

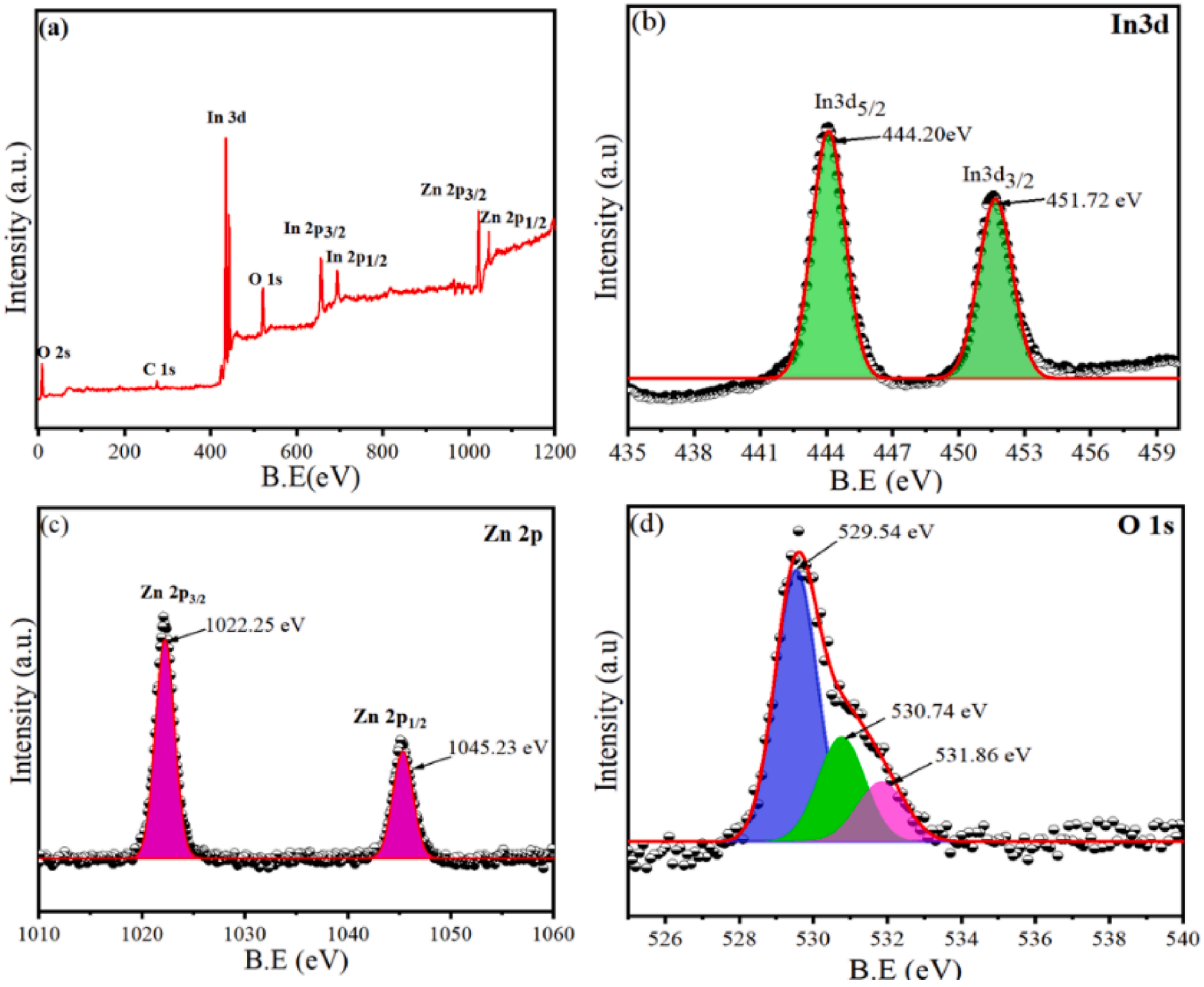

Fig. 5. XPS Characterization of Zn (7.5 mol%)-doped In_2O_3 NPs: (a) Full scan of XPS spectra, (b) XPS spectra of In3d, (c) XPS spectra of Zn2p, and (d) XPS spectra of O 1s.

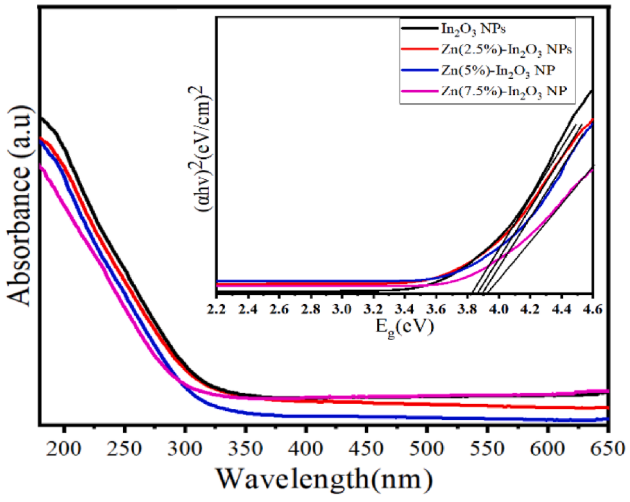

Fig. 6. UV spectra of undoped In_2O_3 NPs and Zn (2.5, 5, and 7.5 mol%)-doped In_2O_3 NPs.

1045.23 eV within the Zn 2p spectra (Fig. 5b) were associated with the Zn $2p_{3/2}$ and Zn $2p_{1/2}$ peaks, respectively. These peaks distinctly represent Zn^{2+}, which serves as a characteristic feature indicating the oxidation state of Zn in prepared Zn-doped In_2O_3 NPs (Sahai and Goswami, 2015). Fig. 5d illustrates XPS spectra of the O1s that exhibited three distinct peaks at 529.54 eV, 530.74 eV, and 531.86 eV. The peak at 529.54 eV is associated with the characteristic lattice oxygen (O_2^-) features originating from the In_2O_3 lattice (Ma et al., 2016). Similarly, the peaks at 530.74 eV and 531.86 eV are ascribed to the oxygen within regions deficient in the crystalline In–Zn–O system (Montazeri and Jamali-Sheini, 2017). XPs results confirmed that Zn dopants into the In_2O_3 NPs were successfully achieved.

3.5. UV–Vis optical Characterization

Fig. 6 shows the absorption of UV spectra of both undoped In_2O_3 NPs and Zn (2.5 %, 5 %, and 7.5 %)-doped In_2O_3 NPs. We observed that there is a slight shift in the absorption edge of peaks for undoped In_2O_3 NPs and Zn-doped In_2O_3 NPs. This phenomenon of blue shift is a consequence of the wider band gap energy in Zn-doped In_2O_3 NPs. The plot of $(\alpha h\nu)^2$ against photon energy ($E_g = h\nu$) was created (Fig. 6) to estimate the band gap energy (Eg) of the NPs. In the present analysis, the energy band gap was estimated using the formula $[(\alpha h\nu)^m = A(hv\text{-}Eg)]$, where Eg is the band gap energy, A is the transition probability-based constant, and m is optical absorption power index (m = 2). We observed that the band gap energies of undoped In_2O_3 NPs and Zn (2.5 %, 5 %, and 7.5 mol %)-doped In_2O_3 NPs were 3.83 eV, 3.86 eV, 3.90 eV, and 3.93 eV, respectively. The band gap values indicate a gradual increase in band gap energy with increasing Zn. However, when Zn doped in In_2O_3 NPs, the electronic states to the band structure of In_2O_3 NPs are created. Thus, dopant-induced states are caused by the transition between the valance

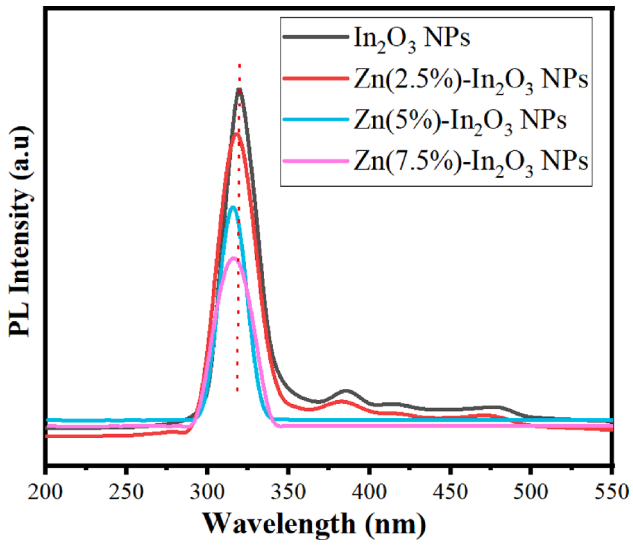

Fig. 7. PL spectra of undoped In_2O_3 NPs and Zn (2.5, 5, and 7.5 mol%)-doped In_2O_3 NPs.

and conduction bands of highest occupied molecular orbitals (HOMO) and lowest unoccupied (LUMO) orbitals(Amini et al., 2014). Due to this transition between HOMO and LUMO orbitals Zn-doped In_2O_3 materials can generate and separate electron-hole pairs efficiently, making them excellent for photocatalytic and anticancer applications. Our results were good matched in from prior examinations (Ahamed et al., 2016; Shanmuga Priya et al., 2017; Shokohmanesh and Jamali-Sheini, 2017b).

3.6. PL analysis

Fig. 7 displays the PL spectra of undoped In_2O_3 NPs and Zn-doped In_2O_3 NPs at 300 nm excitation wavelength. PL spectra showed that emission peaks of undoped In_2O_3 NPs and Zn (2.5, 5, and 7.5 mol %)-doped In_2O_3 NPs were 322.8 nm, 321.3 nm, 318 nm, and 315.2 nm, respectively, corresponding to their band gap energy. This shift in emission peaks is attributed to the addition of Zn ions in the In_2O_3 crystal lattice (Singh et al., 2010). Besides, the weak emission peaks were assigned at around 390.1 nm and 415 nm, which could be owing to the existence of oxygen vacancies or interstitial zinc ions (Saikia et al., 2015). A significant shift to a lower wavelength was further observed with the addition of Zn ions. Likewise, there is a significant decrease in the Peak emission intensity with increasing Zn concertation due to occupying Zn^{2+} ions instead of O_2^- ion sites in the In_2O_3 crystal lattice (Alexandrov et al., 2020). PL emission spectra were good in agreement with an earlier study (Almontasser and Parveen, 2020). These results indicated that the Zn-doped In_2O_3 NPs can be used in enhanced photocatalytic and anticancer performance.

3.7. Cytotoxicity study

Several oxide NPs with metal ions are attracted to potential uses for cancer therapy applications (Du et al., 2022; Fu et al., 2017; Vinardell and Mitjans, 2018). Fig. 8(a and b) illustrate the cell viability of MCF-7 and HCT116 cells using the MTT assay for undoped In_2O_3 NPs and Zn-doped In_2O_3 NPs. As shown in Fig. 8a, both undoped In_2O_3 NPs and Zn-doped In_2O_3 NPs exhibited a dose-dependent cytotoxicity influence toward MCF-7 cancer cells. Results exhibited (Fig. 8a) that the cytotoxicity effect of undoped In_2O_3 NPs against MCF-7 cancer cells was increased proportionally with increasing amounts of Zn doping. Similarly, the Zn-doped In_2O_3 NPs induced high cytotoxicity (Fig. 8b) at

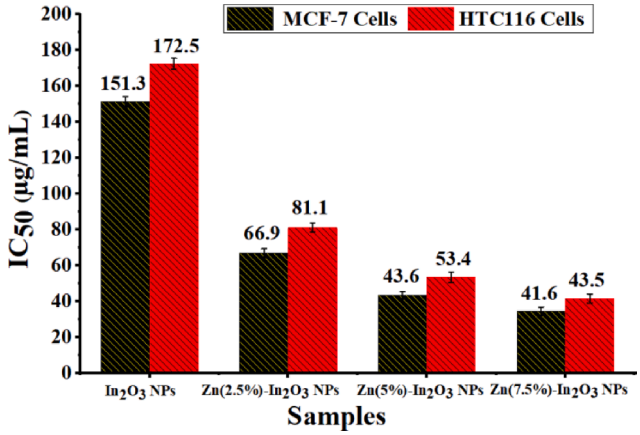

Fig. 9. Inhibitory concentration (IC_{50}) for undoped In_2O_3 NPs and Zn (2.5, 5, and 7.5 mol%)-doped In_2O_3 NPs against two cancer cell lines (MCF-7 and HCT116).

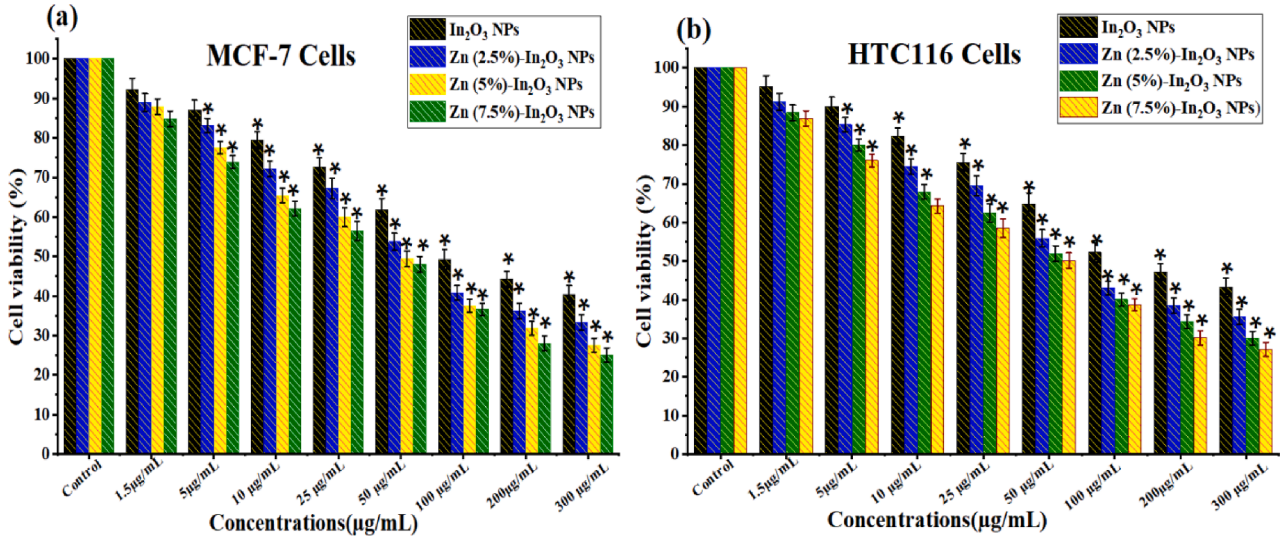

Fig. 8. Cellular viability assessment of undoped In_2O_3 NPs and Zn (2.5 %, 5 %, and 7.5 mol%)-doped In_2O_3 NPs using the MTT Assay: Cell viability in (a) MCF-7 cells and (b) HCT116 cells following exposure to different Concentrations (1.5–300 µg/mL) of each NPs for 24 h. * Shows a statistically significant difference from the control group ($p < 0.05$).

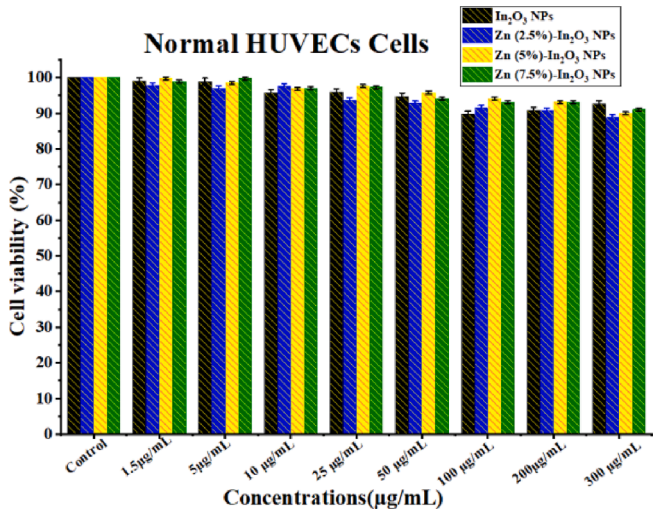

Fig. 10. Biocompatibility assay of normal HUVECs for 24 h exposure with different Concentrations (1.5–300 µg/mL) of each undoped In_2O_3 NPs and Zn (2.5 %, 5 %, and 7.5 mol%)-doped In_2O_3 NPs.

higher concentrations toward HCT116 cells than undoped In_2O_3 NPs. Notably, the inhibitory concentration (IC_{50}) for undoped In_2O_3 NPs and Zn-doped In_2O_3 NPs on MCF-7 and HCT116 cancer cells were shown in Fig. 9. It shows that breast cancer cells (MCF-7) exhibited more sensitivity to the cytotoxic effects of both undoped and Zn-doped In_2O_3 NPs compared to HCT116 cells. These results suggest that the anticancer efficacy of Zn-doped In_2O_3 NPs enhanced in comparison to In_2O_3 NPs owing to Zn^{2+} ion addition.

Our previous studies suggest the potential mechanisms of cancer death by NPs (Ahamed et al., 2021; Alaizeri et al., 2022a) In the present work, Zn-doped In_2O_3 NPs generate reactive oxygen species (ROS) inside cancer cells due react Zn^{2+} ion and In^{3+}ion with molecules of cells (Fenton reaction). Hence, ROS includes a group of chemicals, including superoxide radicals ($O^{\cdot}_2$) and hydrogen peroxide ($^{\cdot}$ OH), that exhibit high reactivity. These free radicals can cause oxidative stress and damage DNA, proteins, and lipids. The presence of oxidative stress can potentially induce apoptosis, which is a regulated process of cell death.

3.8. Biocompatibility study

Human normal cells are used to assess the biocompatibility of potential anticancer agents. The present study assessed biocompatibility (Fig. 10) on HUVE normal cells at different concentrations (1.5 to 300 µg/mL) for synthesized samples. Fig. 10 indicates that the presence of undoped In_2O_3 NPs and Zn (2.5 %, 5 %, and 7.5 %)-doped In_2O_3 NPs did not influence the normal HUVECs. It can be observed that the biocompatibility of In_2O_3 NPs shows enhancement with increasing Zn doping. These results revealed that the Zn (2.5 %, 5 %, and 7.5 %)-doped In_2O_3 NPs can selectively eradicate cancer cells with no effect on normal cells. Based on these results, the biocompatibility of these NPs can be determined by a safe range of concentrations for the potential vivo model. These results were excellent in agreement with previous studies for metal-doped oxide nanoparticles (Ahamed and Khan, 2023; Alaizeri et al., 2021).

4. Conclusions

In this work, the precipitation process was used to effectively produce both undoped In_2O_3 NPs and Zn (2.5, 5, 7.5 mol%)-doped In_2O_3 NPs. The present work showed several advantages of using these NPs for biomedical applications including, including low toxicity, a cost-effective, and scalable approach. This study focused on Zn doping In_2O_3 NPs to improve their anticancer properties. The physicochemical properties of synthesized materials were investigated using XRD, TEM, SEM, EDX, XPS, UV–Vis, and PL spectroscopy. XRD analysis showed that Zn doping affected the crystalline structure and phase composition of produced undoped In_2O_3 NPs. TEM and SEM analysis show that the produced NPs exhibited spherical morphology and homogeneous distribution. The elements (Zn, In, and O) and their distribution in Zn-doped In_2O_3 NPs were verified by EDX and XPS analysis. UV–Vis data showed that the band gap energies of prepared samples were increased from 3.38 eV to 3.93 eV with increasing Zn amount. PL peak emissions of prepared samples were observed at around 322.5 nm, 390.1 nm, and 417.6 nm. MTT analysis demonstrated that the cytotoxicity of undoped In_2O_3 NPs against MCF-7 and HCT116 cancer cells was increased with increasing Zn concentration, while normal human cells (HUVECs) did not affect. These results reveal that Zn doping plays a role as therapeutic agent in cancer therapy. The results suggest that these NPs could hold promise as a targeted therapeutic strategy in vivo model.

Consent to participate or publication: N/A.

Declarations: This manuscript is an original investigation; also, it is not submitted elsewhere for publication.

Declaration of competing interest

The authors declare that they have no known competing financial interests or personal relationships that could have appeared to influence the work reported in this paper.

Acknowledgment

The authors extend their sincere appreciation to researchers supporting project number (RSPD2023R813), King Saud University, Riyadh, Saudi Arabia for funding this research.

Appendix A. Supplementary material

Supplementary data to this article can be found online at https://doi.org/10.1016/j.jksus.2023.103015.

References

Ahamed, M., Akhtar, M.J., Khan, M.A.M., Alaizeri, Z.M., Alhadlaq, H.A., 2021. Facile Synthesis of Zn-Doped Bi_2O_3 Nanoparticles and Their Selective Cytotoxicity toward Cancer Cells. ACS Omega 6, 17353–17361.

Ahamed, M., Khan, M.A.M., 2023. Enhanced Photocatalytic and Anticancer Activity of Zn-Doped $BaTiO_3$ Nanoparticles Prepared through a Green Approach Using Banana Peel Extract. Catalysts 13, 985. https://doi.org/10.3390/catal13060985.

Ahamed, M., Khan, M.A.M., Akhtar, M.J., Alhadlaq, H.A., Alshamsan, A., 2016. Role of Zn doping in oxidative stress mediated cytotoxicity of TiO_2 nanoparticles in human breast cancer MCF-7 cells. Sci. Rep. 6, 1–11. https://doi.org/10.1038/srep30196.

Ahmed, A.A.A., Alahsab, E.A.A., Abdulwahab, A.M., 2021. The influence of Zn and Mg doping on the structural and optical properties of NiO nano-structures for optoelectronic applications. Results Phys. 22, 103938 https://doi.org/10.1016/j.rinp.2021.103938.

Alahsab, E.A.A., Ahmed, A.A.A., Abdulwahab, A.M., 2023. Synthesis, Structural, Optical and Electrical Properties of Pure and Doped NiO Nanostructures Prepared via The Co-precipitation Method. Thamar Univ. J. Nat. Appl. Sci. 8, 56–69. https://doi.org/10.59167/tujnas.v8i1.1491.

Alaizeri, Z.M., Alhadlaq, H.A., Aldawood, S., Akhtar, M.J., Amer, M.S., Ahamed, M., 2021. Facile synthesis, characterization, photocatalytic activity, and cytotoxicity of ag-doped mgo nanoparticles. Nanomaterials 11. https://doi.org/10.3390/nano11112915.

Alaizeri, Z.A.M., Alhadlaq, H.A., Aldawood, S., Akhtar, M.J., Ahamed, M., 2022a. Photodeposition mediated synthesis of silver-doped indium oxide nanoparticles for improved photocatalytic and anticancer performance. Environ. Sci. Pollut. Res. https://doi.org/10.1007/s11356-022-22594-9.

Alaizeri, Z.M., Alhadlaq, H.A., Aldawood, S., Javed, M., Maqusood, A., 2022b. Photodeposition mediated synthesis of silver - doped indium oxide nanoparticles for improved photocatalytic and anticancer performance. Environ. Sci. Pollut. Res. https://doi.org/10.1007/s11356-022-22594-9.

Alexandrov, A., Zvaigzne, M., Lypenko, D., Nabiev, I., Samokhvalov, P., 2020. Al-, Ga-, Mg-, or Li-doped zinc oxide nanoparticles as electron transport layers for quantum dot light-emitting diodes. Sci. Rep. 10, 1–11. https://doi.org/10.1038/s41598-020-64263-2.

Almontasser, A., Parveen, A., 2020. Synthesis and characterization of indium oxide nanoparticles. AIP Conf. Proc. 2220 https://doi.org/10.1063/5.0001683.

Amini, M.N., Dixit, H., Saniz, R., Lamoen, D., Partoens, B., 2014. The origin of p-type conductivity in ZnM2O4 (M = Co, Rh, Ir) spinels. Phys. Chem. Chem. Phys. 16 (6), 2588–2596.

Ayeshamariam, A., Kashif, M., Bououdina, M., Hashim, U., Jayachandran, M., Ali, M.E., 2014. Morphological, structural, and gas-sensing characterization of tin-doped indium oxide nanoparticles. Ceram. Int. 40, 1321–1328. https://doi.org/10.1016/j.ceramint.2013.07.012.

Bierwagen, O., 2015. Indium oxide—a transparent, wide-band gap semiconductor for (opto)electronic applications. Semicond. Sci, Technol, p. 30.

Bouhdjer, A., Saidi, H., Attaf, A., Aida, M.S., JlassI, M., Bouhaf, I., Benkhetta, Y., Bendjedidi, H., 2016. Structural, morphological, optical, and electrical properties of In2O3 nanostructured thin films. Optik (Stuttg). 127, 7319–7325. https://doi.org/10.1016/j.ijleo.2016.05.035.

Darvish, M., Nasrabadi, N., Fotovat, F., Khosravi, S., Khatami, M., Jamali, S., Mousavi, E., Iravani, S., Rahdar, A., 2022. Biosynthesis of Zn-doped CuFe(2)O(4) nanoparticles and their cytotoxic activity. Sci. Rep. 12, 9442. https://doi.org/10.1038/s41598-022-13692-2.

Du, H., Akakuru, O.U., Yao, C., Yang, F., Wu, A., 2022. Transition metal ion-doped ferrites nanoparticles for bioimaging and cancer therapy. Transl. Oncol. 15, 101264 https://doi.org/10.1016/j.tranon.2021.101264.

Fu, C., Zhou, H., Tan, L., Huang, Z., Wu, Q., Ren, X., Ren, J., Meng, X., 2017. Microwave-{Activated} Mn}-{Doped {Zirconium} Metal}–{Organic {Framework} Nanocubes for Highly {Effective} Combination of Microwave {Dynamic} and Thermal {Therapies} Against {Cancer}. ACS Nano 12, 2201–2210. https://doi.org/10.1021/acsnano.7b08868.

Gao, P., Pan, W., Li, N., Tang, B., 2019. Boosting Cancer {Therapy} with Organelle}-{Targeted {Nanomaterials}. ACS Appl. Mater. & Interfaces 11, 26529–26558. https://doi.org/10.1021/acsami.9b01370.

Huang, B., Lin, J.-C., 2012. Core–shell structure of zinc oxide/indium oxide nanorod based hydrogen sensors. Sensors Actuators B-chem. 174, 389–393.

Inyawilert, K., Channei, D., Tamaekong, N., Liewhiran, C., Wisitsoraat, A., Tuantranont, A., Phanichphant, S., 2016. Pt-doped In2O3 nanoparticles prepared by flame spray pyrolysis for NO2 sensing. J. Nanoparticle Res. 18 https://doi.org/10.1007/s11051-016-3341-1.

Jahan, I., 2022. Nanotechnology for {Drug} {Delivery} and {Cancer} {Therapy}, in: Handbook of {Research} on {Green} {Synthesis} and {Applications} of {Nanomaterials}. IGI Global, pp. 338–362. https://doi.org/10.4018/978-1-7998-8936-6.ch015.

Karmaoui, M., Leonardi, S.G., Latino, M., Tobaldi, D.M., Donato, N., Pullar, R.C., Seabra, M.P., Labrincha, J.A., Neri, G., 2016. Pt-decorated In2O3nanoparticles and their ability as a highly sensitive (<10 ppb) acetone sensor for biomedical applications. Sensors and Actuators B-chemical 230, 697–705.

Khan, M.A.M., Siwach, R., Kumar, S., Ahmed, J., Ahamed, M., 2020. Hydrothermal preparation of Zn-doped In_2O_3 nanostructure and its microstructural, optical, magnetic, photocatalytic and dielectric behaviour. J. Alloys Compd. 846, 156479 https://doi.org/10.1016/j.jallcom.2020.156479.

Koo, B.R., Park, I.K., Ahn, H.J., 2014. Fe-doped In_2O_3/α-Fe_2O_3 core/shell nanofibers fabricated by using a co-electrospinning method and its magnetic properties. J. Alloys Compd. 603, 52–56. https://doi.org/10.1016/j.jallcom.2014.03.058.

Kulkarni, S.C., Patil, D.S., 2016. Synthesis and characterization of uniform spherical shape nanoparticles of indium oxide. J. Mater. Sci. Mater. Electron. 27, 3731–3735. https://doi.org/10.1007/s10854-015-4215-5.

Li, H., Chen, Z., Li, J., Liu, R.u., Zhao, F., Liu, R., 2020. Indium oxide nanoparticles induce lung intercellular toxicity between bronchial epithelial cells and macrophages. J. Appl. Toxicol. 40, 1636–1646. https://doi.org/10.1002/jat.4023.

Li, P., Fan, H., Cai, Y., Xu, M., Long, C., Li, M., Lei, S., Zou, X., 2014. Phase transformation (cubic to rhombohedral): the effect on the NO2 sensing performance of Zn}-doped flower-like { In2O3 structures. RSC Adv. 4, 15161. https://doi.org/10.1039/c3ra47467d.

Ma, L., Fan, H., Tian, H., Fang, J., Qian, X., 2016. The n-ZnO/n- In_2O_3 heterojunction formed by a surface-modification and their potential barrier-control in methanal gas sensing. Sensors Actuators B. Chem. Complete 508–516. https://doi.org/10.1016/J.SNB.2015.08.085.

Malini, V.H., B, I., Gunasekhar, R., Prabu, A.A., 2022. A Review on Electrospun PVDF-Doped Metal Oxide Nanoparticles for Sensor Applications. ECS Trans.

Martha, S., Reddy, K.H., Parida, K.M., 2014. Fabrication of In2O3 modified ZnO for enhancing stability, optical behaviour, electronic properties and photocatalytic activity for hydrogen production under visible light. J. Mater. Chem. A 2, 3621. https://doi.org/10.1039/c3ta14285j.

Mishra, P.K., Mishra, H., Ekielski, A., Talegaonkar, S., Vaidya, B., 2017. Zinc oxide nanoparticles: a promising nanomaterial for biomedical applications. Drug Discov. Today 22, 1825–1834. https://doi.org/10.1016/j.drudis.2017.08.006.

Montazeri, A., Jamali-Sheini, F., 2017. Enhanced ethanol gas-sensing performance of Pb-doped In_2O_3 nanostructures prepared by sonochemical method. Sensors Actuators, B Chem. 242, 778–791. https://doi.org/10.1016/j.snb.2016.09.181.

Naik, M.Z., Salker, A.V., 2017. A systematic study of cobalt doped In_2O_3 nanoparticles and their applications. Mater. Res. Innov. 21, 237–243.

Navya, P.N., Kaphle, A., Srinivas, S.P., Bhargava, S.K., Rotello, V.M., Daima, H.K., 2019. Current trends and challenges in cancer management and therapy using designer nanomaterials. Nano Converg. 6 https://doi.org/10.1186/s40580-019-0193-2.

Patel, S., Nanda, R., 2015. Nanotechnology in {Healthcare}: Applications and {Challenges}. Med. Chem. (Los. Angeles). 05 https://doi.org/10.4172/2161-0444.1000312.

Sahai, A., Goswami, N., 2015. Structural and optical investigations of oxygen defects in zinc oxide nanoparticles. AIP Conf. Proc. 1665, 1–4. https://doi.org/10.1063/1.4917664.

Saikia, L., Bhuyan, D., Saikia, M., Malakar, B., Dutta, D.K., Sengupta, P., 2015. Photocatalytic performance of ZnO nanomaterials for self sensitized degradation of malachite green dye under solar light. Appl. Catal. A Gen. 490, 42–49. https://doi.org/10.1016/j.apcata.2014.10.053.

Samerjai, T., Channei, D., Khanta, C., Inyawilert, K., Liewhiran, C., Wisitsoraat, A., Phokharatkul, D., Phanichphant, S., 2016. Flame-spray-made ZnInO alloyed nanoparticles for NO2 gas sensing. J. Alloys Compd. 680, 711–721.

Shanmuga Priya, B., Shanthi, M., Manoharan, C., Dhanapandian, S., 2017. Synthesis, characterization and photocatalytic activity of pure and Zn-doped In_2O_3 nanostructures. J. Mater. Sci. Mater. Electron. 28, 12784–12794. https://doi.org/10.1007/s10854-017-7106-0.

Shanmuganathan, V., Santhosh Kumar, J., Pachaiappan, R., Thangadurai, P., 2021. Transition metal ion-doped In_2O_3 nanocubes: investigation of their photocatalytic degradation activity under sunlight. Nanoscale Adv. 3, 471–485. https://doi.org/10.1039/d0na00694g.

Sharma, A., Saini, A.K., Kumar, N., Tejwan, N., Singh, T.A., Thakur, V.K., Das, J., 2022. Methods of preparation of metal-doped and hybrid tungsten oxide nanoparticles for anticancer, antibacterial, and biosensing applications. Surfaces and Interfaces 28, 101641. https://doi.org/10.1016/j.surfin.2021.101641.

Sheena, P.A.L., Sreedevi, A., Viji, C., Thomas, V., 2019. Nickel oxide/cobalt phthalocyanine nanocomposite for potential electronics applications. Eur. Phys. J. B 92, 1–8.

Shokohmanesh, A., Jamali-Sheini, F., 2017. Synthesis and transient photocurrent behavior of Zn-doped In_2O_3 nanorods. Sensors Actuators A Phys. 265, 246–252. https://doi.org/10.1016/j.sna.2017.08.010.

Singh, N., Yan, C., Lee, P.S., 2010. Room temperature CO gas sensing using Zn-doped In_2O_3 single nanowire field effect transistors. Sensors Actuators B Chem. 150, 19–24. https://doi.org/10.1016/j.snb.2010.07.051.

Sun, T., Zhang, Y.S., Pang, B., Hyun, D.C., Yang, M., Xia, Y., 2014. Engineered {Nanoparticles} for {Drug} {Delivery} in {Cancer} {Therapy}. Angew. Chemie Int. Ed. n/a–n/a. https://doi.org/10.1002/anie.201403036.

Sun, X., Liu, X., Deng, X., Xu, X., 2016. Synthesis of Zn-doped In_2O_3 nanosphere architectures as a triethylamine gas sensor and photocatalytic properties. RSC Adv. 6, 89847–89854. https://doi.org/10.1039/c6ra16789f.

Vázquez-Olmos, A.R., Gómez-Peralta, J.I., Sato-Berrú, R.Y., FERNÁNDEZ-OSORIO, A.L., 2014. Diluted magnetic semiconductors based on Mn-doped In2O3 nanoparticles. J. Alloys Compd. 615.

Vinardell, M.P., Mitjans, M., 2018. Metal/{Metal} {Oxide} {Nanoparticles} for {Cancer} {Therapy}, in: Nanooncology. Springer International Publishing, pp. 341–364. https://doi.org/10.1007/978-3-319-89878-0_10.

Yan, S., Li, Z., Li, H., Wu, Z., Wang, J., Shen, W., Fu, Y.Q., 2018. Ultra-sensitive room-temperature H2S sensor using Ag–In2O3 nanorod composites. J. Mater. Sci. 53, 16331–16344. https://doi.org/10.1007/s10853-018-2789-z.

Yang, Y.-C., Niu, J.-S., Liu, W.-C., 2022. Study of a Palladium Nanoparticle/Indium Oxide-Based Hydrogen Gas Sensor. IEEE Trans. Electron Devices 69, 318–324.

Zhang, S., Song, P., Yan, H., Wang, Q., 2016. Self-assembled hierarchical Au-loaded In2O3 hollow microspheres with superior ethanol sensing properties. Sensors Actuators, B Chem. 231, 245–255. https://doi.org/10.1016/j.snb.2016.03.020.

Zhang, W.H., Zhang, W.D., 2012. Biomolecule-assisted synthesis and gas-sensing properties of porous nanosheet-based corundum In_2O_3 microflowers. J. Solid State Chem. 186, 29–35. https://doi.org/10.1016/j.jssc.2011.11.031.

Zhao, Q.G., Wang, J., Zhang, Y.P., Zhang, J., Tang, A.N., Kong, D.M., 2018. A ZnO-gated porphyrinic metal-organic framework-based drug delivery system for targeted bimodal cancer therapy. J. Mater. Chem. B 6, 7898–7907. https://doi.org/10.1039/c8tb02663g.

Zheng, Q., Lee, J.H., Kim, S.J., Lee, H.S., Lee, W., 2021. Excellent isoprene-sensing performance of In_2O_3 nanoparticles for breath analyzer applications. Sensors Actuators, B Chem. 327, 128892 https://doi.org/10.1016/j.snb.2020.128892.

Zhu, W., Xu, T., Liu, W., Wang, W., Feng, M., Cheng, Y., Li, Y., Tian, Y., Li, X., 2020. High-performance ethanol sensor based on In_2O_3 nanospheres grown on silicon nanoporous pillar array. Sensors Actuators B Chem. 324, 128734 https://doi.org/10.1016/j.snb.2020.128734.